

# Hydrodynamic Behavior of Non-spherical Particles in Confined Vertical Flows: A Resolved CFD-DEM Study

Amiya Prakash Das<sup>a</sup>, Shakti Swaroop Choudhury<sup>a</sup>, Sujith Reddy Jaggannagari<sup>a</sup>, Amudha Krishnan<sup>b</sup>, Gopkumar Kuttikrishnan<sup>b</sup>, Ratna Kumar Annabattula<sup>a,\*</sup>

<sup>a</sup>*Mechanics of Materials Lab, Department of Mechanical Engineering, Indian Institute of Technology Madras, Chennai, 600036, Tamil Nadu, India*

<sup>b</sup>*Deep Sea Mining, National Institute of Ocean Technology, Chennai, 600100, Tamil Nadu, India*

---

## Abstract

We investigate the sedimentation and vertical hydraulic transport of irregular polymetallic nodules (PMNs) using resolved CFD-DEM with multisphere particles spanning  $100 < Re_p < 3000$ . Shape effects induce 2.0-2.3 times drag enhancement relative to volume-equivalent spheres, arising from 50% larger frontal areas and wake asymmetry, reducing terminal velocities by 29-33%. Vertical transport exhibits velocity-driven transitions from intermittent settling to stable convection, as demonstrated by residence-time and drag-force statistics. While PMNs exhibit enhanced rotational-translational coupling and broader force fluctuations, the regime progression qualitatively resembles that of volume-equivalent spherical particles. Drag variance evolution reveals contrasting behavior: small particles ( $d/D = 0.082$ ) show narrow distributions and wake suppression at higher velocities, while large particles ( $d/D = 0.22$ ) exhibit non-monotonic variance. These findings elucidate shape-confinement interactions in vertical transport and establish bounds on the applicability of volume-equivalent spherical particles in reduced-order models.

**Keywords:** Non-spherical Particles; Immersed Boundary Method; CFD-DEM; Deep-sea Mining; Polymetallic Nodules

---

## 1 Introduction

The recovery of polymetallic nodules (PMNs) from abyssal plains relies on hydraulic systems to transport coarse non-spherical particles through vertical risers extending several kilometers [Hein et al., 2020, Leng et al., 2021]. The efficiency of these systems depends on the ability to predict particle entrainment, suspension stability, and transport behavior under strong gravitational forcing and geometric confinement [Van Wijk et al., 2016, Dai et al., 2024, Su et al., 2024, Chen et al., 2025, Yang et al., 2025]. In such risers, particles are often comparable in size to the riser diameter and interact strongly with both the carrier fluid and the confining walls, leading to complex multiphase flow behavior [Shen et al., 2022, Schnorr Filho et al., 2022, Zhao et al., 2022, Sun et al., 2025, Yang et al., 2025].

Hydraulic collection systems are favored in deep-sea mining operations for their operational efficiency and mechanical simplicity [Liu et al., 2023, Li et al., 2024, Zhang et al., 2024]. These systems rely on fluid entrainment to transport PMNs through vertical risers, a

---

\*Corresponding author

Email addresses: [apdas@connect.ust.hk](mailto:apdas@connect.ust.hk) (Amiya Prakash Das), [ratna@iitm.ac.in](mailto:ratna@iitm.ac.in) (Ratna Kumar Annabattula)

process governed by the hydrodynamic behavior of coarse, non-spherical particles in dense slurries [Zhou et al., 2010, 2011, Elskamp et al., 2017, Fan et al., 2024, Chen et al., 2025, Huang et al., 2025]. However, the hydraulic transport of PMNs differs fundamentally from particle-laden flow owing to strong confinement effects, particle size, and morphology. Unlike spherical particles, PMNs exhibit complex particle-flow interactions characterized by enhanced drag, shape-dependent lift forces, coupled rotational-translational motion, and altered settling dynamics [Haider and Levenspiel, 1989, Ganser, 1993, Hölzer and Sommerfeld, 2008, Chen et al., 2020]. These shape effects significantly influence transport efficiency, minimum suspension velocity, and energy consumption. The particle-shape effects have been extensively studied in unconfined and weakly confined flows [Diamant, 2009, Suresh and Kannan, 2011, Bagheri and Bonadonna, 2016, Cheng et al., 2023]. Their role in narrow vertical risers with high confinement ratios ( $d/D \geq 0.2$ ), representative of deep-sea mining risers, remains underexplored.

Existing numerical studies of hydraulic transport use unresolved CFD-DEM frameworks, in which particle-fluid interactions are modeled using empirical drag correlations [Di Felice, 1994, Zhao and Shan, 2013]. These correlations are primarily calibrated for spherical particles and do not capture the mesoscale physics associated with surface morphology of non-spherical particles, like orientation-dependent drag, wake asymmetry, and rotational coupling [Hölzer and Sommerfeld, 2008, Malone and Xu, 2008, Nan et al., 2022, Cheng et al., 2023]. The limitations of unresolved approaches are particularly pronounced in highly confined flows, where particle-fluid and particle-wall interactions dominate the transport dynamics and may trigger flow instabilities, intermittent settling, and jamming [Sommerfeld, 1992, Aponte-Rivera and Zia, 2016, Chen and Li, 2020]. Resolved CFD-DEM offers a physically robust alternative by explicitly resolving particle-fluid interactions at the interface without relying on empirical closures [Luo et al., 2007, Lu et al., 2018, Yan et al., 2025]. Recent studies have demonstrated the ability of resolved CFD-DEM to capture shape effects and confinement-induced transport phenomena in narrow risers, including shear jamming, wake-mediated interactions, and regime transitions [Cunez and Franklin, 2019, Cúñez and Franklin, 2020, Schnorr Filho et al., 2022]. Advancements in geometric representation using signed distance functions (SDF) and multisphere approximations have further enhanced the adaptability of these methods for modeling arbitrarily shaped particles [Shen et al., 2022, Lai et al., 2023]. These developments establish resolved CFD-DEM as a robust tool for investigating mesoscale particle-fluid interactions, which are critical to engineering applications [Nan et al., 2023, Hu et al., 2024].

Despite advancements, resolved CFD-DEM for industrial-scale riser simulations remains computationally prohibitive. Resolving realistic PMN surface morphology for  $\mathcal{O}(10^3 - 10^4)$  particles using SDF/multisphere over large-scale domains requires substantial CPU hours, making parametric design intractable. Consequently, large-scale simulations often resort to spherical representations, achieving order-of-magnitude reductions in CPU hours at the expense of morphological fidelity. This raises a critical question: can volume-equivalent spheres accurately reproduce the transport behavior of realistic PMNs, or do shape effects persist at the ensemble level? Addressing this requires systematic validation that isolates shape-induced hydrodynamic effects from collective phenomena such as dense-phase interactions and polydispersity, a distinction obscured in fully representative industrial simulations. The present study employs a controlled vertical transport configuration with moderate particle ensembles, enabling direct comparison of X-ray computed tomography (CT) reconstructed PMNs with volume-equivalent spherical particles under identical flow conditions.

In this work, we employ resolved CFD-DEM to investigate the hydrodynamic behavior

of non-spherical PMNs in vertical pipes representative of deep-sea mining risers. The model couples the incompressible Navier-Stokes equations with Newton's equations of motion for discrete particles, whose irregular geometries are represented using multisphere approximations derived from CT scans. We systematically analyze the influence of particle-to-pipe diameter ratio, particle Reynolds number, and flow velocity on particle trajectories, residence time distributions, and drag force statistics. Residence time analysis characterizes the transition from settling-dominated to convection-dominated transport, enabling prediction of minimum suspension velocities [Chen et al., 2019, Lan et al., 2020], while drag force statistics reveal underlying force balance mechanisms. The objectives are twofold: first, to elucidate mechanisms by which particle shape influences drag, wake dynamics, and rotational-translational coupling in confined vertical flows; and second, to assess whether ensemble-averaged transport metrics for non-spherical PMNs qualitatively converge toward those of volume-equivalent spheres, thereby establishing when spherical models are suitable for reduced-order simulations of large-scale hydraulic transport systems.

The remainder of this paper is structured as follows. [Section 2](#) presents the mathematical formulation of the resolved CFD-DEM framework, detailing the Navier-Stokes equations for the fluid phase, Newton's equations for particle dynamics, the immersed boundary method for fluid-solid coupling, and the multisphere representation for complex geometries. [Section 3](#) presents numerical verification through comparisons with benchmark experiments for spherical and non-spherical particle sedimentation, establishing the model's accuracy across the Stokes-to-intermediate Reynolds number regime. In addition, we have used the classical DKT problem to resolve multiple particle interactions using CFD-DEM framework. [Section 4](#) discussion presents results in two parts: sedimentation analysis, which quantifies the effects of shape on drag coefficients and terminal velocities; and vertical transport simulations that analyze entrainment dynamics, residence time distributions, and drag force statistics as functions of flow velocity and confinement ratio. [Section 5](#) summarizes key findings and discusses implications for hydraulic transport in deep-sea mining applications.

## 2 Methodology

We employ a resolved CFD-DEM framework to investigate the hydraulic transport of coarse, non-spherical PMNs in a vertical cylindrical pipe. The framework couples the Immersed Boundary (IB) method with CFD-DEM, integrating OpenFOAM for fluid dynamics simulation and LIGGGHTS for discrete particle tracking [Kloss and Goniva, 2010]. This fully resolved, bidirectional coupling framework captures the complex multiphase interactions between fluid flow, particle transport, and sedimentation dynamics by resolving meso-scale physics at the fluid-solid interface through a Lagrangian-Eulerian formulation.

### 2.1 Discrete Element Method for Particle Dynamics

Individual particles are modeled within a Lagrangian framework using DEM, where Newton's second law governs each particle's motion for both translational and rotational dynamics

$$m_i \frac{d\mathbf{u}_i}{dt} = m_i \mathbf{g} + \sum_{j \neq i}^{N_c} \mathbf{F}_{c,ij} + \sum_k^{N_w} \mathbf{F}_{c,ik} + \mathbf{F}_{f,i}, \quad (1)$$

$$\mathbb{I}_i \frac{d\omega_i}{dt} = \sum_{j \neq i}^{N_c} \mathbf{T}_{c,ij} + \sum_k^{N_w} \mathbf{T}_{c,ik}, \quad (2)$$

where  $m_i$  and  $\mathbb{I}_i$  represent the mass and moment of inertia tensor of particle  $i$ ,  $\mathbf{u}_i$  and  $\omega_i$  denote linear and angular velocity vectors,  $\mathbf{g}$  is the gravitational acceleration vector,

$\mathbf{F}_{c,ij}$  and  $\mathbf{T}_{c,ij}$  are contact forces and torques between particles  $i$  and  $j$ ,  $\mathbf{F}_{c,ik}$  and  $\mathbf{T}_{c,ik}$  represent wall-particle interactions with wall  $k$ , and  $\mathbf{F}_{f,i}$  is the particle-fluid interaction force computed via the IB method. The particle-particle and particle-wall contact forces are computed using the Hertz-Mindlin contact model with Coulomb friction, which provides an accurate representation of non-linear deformation and energy dissipation during collisions between non-spherical particles [Mindlin and Deresiewicz, 1953, Hager et al., 2012]. The contact detection algorithm efficiently handles complex particle geometries represented as multisphere assemblies.

## 2.2 Computational Fluid Dynamics Formulation

The continuous fluid phase is resolved using an Eulerian framework based on the incompressible Navier-Stokes equations within the fluid domain  $\Omega_f$ , using Equations (3) and (4)

$$\nabla \cdot \mathbf{u}_f = 0, \quad (3)$$

$$\frac{\partial \mathbf{u}_f}{\partial t} + (\mathbf{u}_f \cdot \nabla) \mathbf{u}_f = -\frac{1}{\rho_f} \nabla p + \nu \nabla^2 \mathbf{u}_f, \quad (4)$$

where  $\mathbf{u}_f$  represents the fluid velocity field,  $p$  is the pressure,  $\rho_f$  is the fluid density, and  $\nu = \mu_f/\rho_f$  is the kinematic viscosity with  $\mu_f$  being the dynamic viscosity. The fluid velocity field is initialized as  $\mathbf{u}_f(\mathbf{x}, t = 0) = \mathbf{u}_0(\mathbf{x})$  in  $\Omega_f$ , with Dirichlet boundary conditions  $\mathbf{u}_f = \mathbf{u}_\Gamma$  imposed at domain boundaries  $\Gamma$ . At the fluid-solid interface  $\Gamma_s$ , the no-slip condition enforces velocity continuity

$$\mathbf{u}_f = \mathbf{u}_s \quad \text{on} \quad \Gamma_s, \quad (5)$$

where  $\mathbf{u}_s$  represents the local solid velocity. The fluid stress tensor is defined as  $\sigma = -p\mathbb{1} + \mu_f(\nabla \mathbf{u}_f + (\nabla \mathbf{u}_f)^T)$ , and the surface traction at the interface is  $\mathbf{t} = \sigma \cdot \mathbf{n}$  with  $\mathbf{n}$  being the outward unit normal vector. The governing equations are discretized using OpenFOAM's finite-volume method with second-order spatial accuracy, and temporal integration employs the Pressure-Implicit with Splitting of Operators (PISO) algorithm for robust pressure-velocity coupling [Shen et al., 2022].

## 2.3 Immersed Boundary Method for Fluid-Solid Coupling

The immersed boundary method provides direct fluid-solid coupling by resolving the interface  $\Gamma_s$  without empirical drag correlations, offering significant advantages over the unresolved CFD-DEM framework in terms of accuracy and physical fidelity [Schnorr Filho et al., 2022]. The no-slip condition (Equation (5)) is enforced through a direct forcing approach that modifies the momentum equation. The total hydrodynamic force acting on particle  $i$  is computed by integrating the fluid stress over the particle surface

$$\mathbf{F}_{f,i} = \int_{\Gamma_{s,i}} \sigma \cdot \mathbf{n} dA \approx \sum_{c \in V_{\Omega_{s,i}}} (-\nabla p + \mu_f \nabla^2 \mathbf{u}_f)_c V_c, \quad (6)$$

where  $V_{\Omega_{s,i}}$  represents the set of fluid cells overlapping with solid domain  $\Omega_{s,i}$ ,  $V_c$  is the volume of cell  $c$ , and the summation extends over all fluid cells influenced by particle  $i$ . This formulation captures pressure (buoyancy), viscous drag, and added mass effects without requiring empirical closure relations [Schnorr Filho et al., 2022, Lai et al., 2023]. Void fraction weighting ensures accurate force distribution across the fluid-solid interface, accounting for partial cell occupancy by solid particles.

To ensure accurate resolution of boundary layers around complex particle geometries, the computational grid satisfies the criterion  $\Delta x/D < 0.1$ , where  $\Delta x$  is the characteristic

grid spacing and  $D$  is the characteristic particle dimension [Shen et al., 2022]. This resolution requirement ensures that the viscous boundary layer and near-wall velocity gradients are properly captured for non-spherical particles across the range of  $Re_p$  investigated. The coupling between CFD and DEM solver occurs at a coupling interval of 10 timesteps, with fluid forces from Equation (6) passed to the DEM solver. The updated particle positions and velocities are communicated back to the CFD domain. This bidirectional feedback maintains momentum conservation across the fluid-solid interface while preserving numerical stability through appropriate time step restrictions based on the Courant-Friedrichs-Lowy (Courant number) condition and particle collision time scales.

#### 2.4 Particle Representation

Complex particle geometries are represented using the multisphere approach, where non-spherical particles are constructed as rigid assemblies of overlapping spherical sub-particles, see Figure 1(a). This approach is computationally efficient and high-fidelity, capturing the essential geometric features that influence particle-fluid interactions and collision dynamics. The void fraction field visualization, see Figure 1(b), demonstrates the approach's capability to resolve complex particle-fluid interfaces within the Eulerian CFD grid.

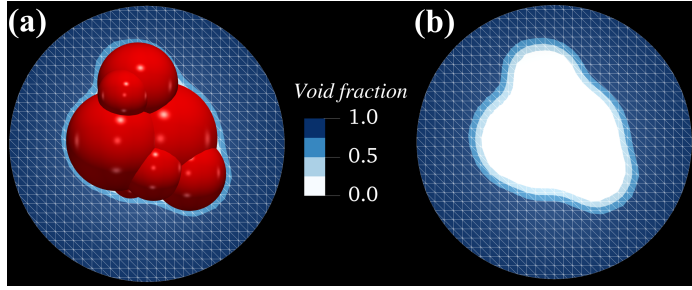


**Figure 1:** Multisphere representation of non-spherical particles in the resolved CFD-DEM framework. (a) Example particle geometry constructed from 14 overlapping spherical sub-particles, demonstrating the multisphere approach for capturing irregular surface features. (b) Corresponding void fraction field distribution in the computational domain, where white regions indicate solid particle volume and blue regions represent pure fluid. The void fraction field resolves the fluid-solid interface within the Eulerian CFD grid, enabling accurate computation of hydrodynamic forces via the IB method without requiring empirical drag correlations.

### 3 Numerical verification

#### 3.1 Single Sphere Settling

The computational framework is verified against experimental data and numerical benchmarks through simulations of a single spherical particle settling in quiescent fluid. We compare our results with the experimental measurements of Ten Cate et al. [2002] and numerical predictions from Lattice Boltzmann Method-DEM (LBM-DEM) [Ten Cate et al., 2002] and CFD-DEM simulations [Lai et al., 2023] to assess the accuracy of terminal velocity predictions within 5% of reference values.

The numerical verification configuration follows the experimental setup of Ten Cate et al. [2002], where a submerged sphere with diameter  $d = 15$  mm and density  $\rho_s = 1120 \text{ kg m}^{-3}$  undergoes free sedimentation within a confined domain of dimensions  $100 \times 100 \times 160 \text{ mm}^3$ . Two test cases with different fluid properties are investigated, as summarized in Table 1, with particles' Reynolds numbers ( $Re_p$ ) spanning from the Stokes regime

to intermediate  $Re_p$  where inertial effects become significant, where  $Re_p = \rho_f u_t d / \mu_f$ . The computational domain is discretized into 819,200 hexahedral cells, with a particle diameter-to-cell ratio of  $d / \Delta x = 12$ , ensuring adequate boundary-layer resolution around the particle. Dynamic mesh refinement is applied locally at the particle-fluid interface to maintain accuracy during particle motion. Time integration employs  $\Delta t_{DEM} = 1 \times 10^{-5}$  s for particle dynamics and  $\Delta t_{CFD} = 1 \times 10^{-4}$  s for fluid flow, with the Courant number maintained below 0.01 for numerical stability. Convergence is monitored through pressure and velocity residuals, with a tolerance of  $10^{-6}$ . [Figure 2](#) presents the temporal evolution of particle velocity for the verification cases, where solid lines represent the CFD-DEM predictions and markers denote experimental measurements. The simulated velocity profiles show good agreement with experimental data throughout the acceleration phase and towards the terminal velocity. Quantitative verification metrics are provided in [Table 1](#), where  $u_{\max}/u_t$  represents the normalized maximum velocity during the initial acceleration phase, and  $Re_p$  is the particles' Reynolds number based on terminal velocity. The maximum deviation between simulated and experimental terminal velocities remains below 10% for the cases, with the  $u_{\max}/u_t$  accurately captured within 10% of experimental values.

**Table 1:** Verification metrics comparing CFD-DEM predictions with experimental data from [Ten Cate et al. \[2002\]](#). Terminal velocity  $u_t$  values are calculated from experimental measurements.

Case	$\rho_f (\text{kg m}^{-3})$	$\mu_f (\text{Pa} \cdot \text{s})$	$u_t (\text{m s}^{-1})^a$	$u_{\max}/u_t$	$Re_p$
Case 1	970	0.373	0.038	0.89	1.3
Case 2	960	0.058	0.128	0.93	29.4

<sup>a</sup>Experimental terminal velocity from [Ten Cate et al. \[2002\]](#)

The flow field snapshots in [Figures 3](#) and [4](#) demonstrate the transition from viscous-dominated to inertia-dominated settling as  $Re_p$  increases. Case 1 ( $Re_p = 1.3$ ) exhibits symmetric streamlines characteristic of Stokes flow, where viscous forces dominate, and inertial effects are negligible. Streamlines smoothly deflect around the particle and reconverge within  $\approx 3.0d$  downstream with no wake formation, see [Figure 3b](#). The velocity field decays smoothly to the far-field value, with the pressure distribution remaining nearly uniform, indicating that viscous shear stress contributes significantly to the total drag. The symmetric flow structure is consistent with the analytical Stokes solution for creeping flow past a sphere.

In contrast, Case 2 ( $Re_p = 29.8$ ) shows flow separation behind the particle with a wake region extending approximately  $1.0d$  downstream. The wake contains slow-moving recirculating fluid, and the pressure in this wake region is lower than upstream, leading to an increased drag contribution due to the pressure difference and lower viscous drag contribution. The transition from symmetric flow to separated flow (see [Figure 4b](#)) occurs as inertial forces become more pronounced relative to viscous forces when  $Re_p$  increases from approximately 1 to 30. The simulated flow patterns agree well with experimental data from [Ten Cate et al. \[2002\]](#). The terminal velocities and wake structures match the experimental measurements within 5%, validating the numerical method across the range  $1 < Re_p < 50$ .

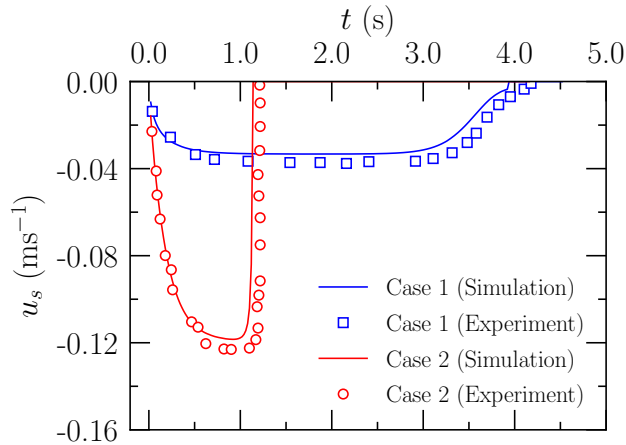


**Figure 2:** Temporal evolution of settling velocity for verification cases comparing CFD-DEM predictions (solid lines) with experimental measurements from [Ten Cate et al. \[2002\]](#) (symbols). The simulations capture both the acceleration phase and the approach to terminal velocity, with an accuracy of 10%, verifying the IB method for hydrodynamic force calculation across the transitional Reynolds number regime.

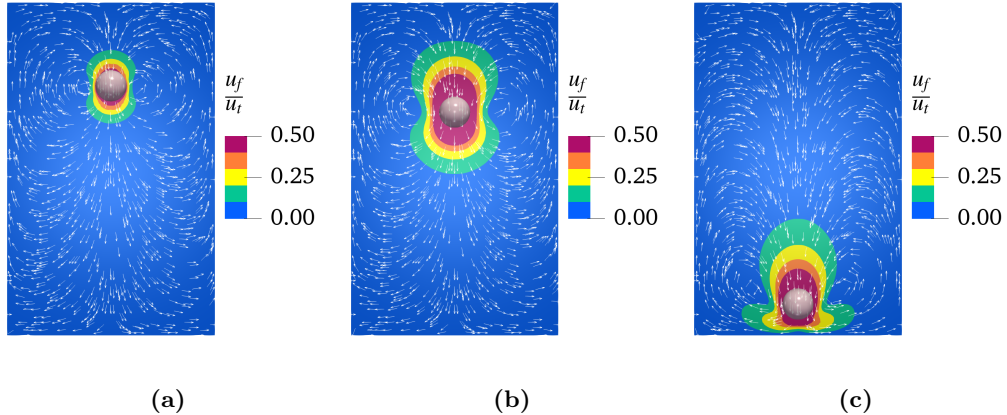


**Figure 3:** Velocity contours and streamlines for  $Re_p = 1.3$  (case 1) showing symmetric flow patterns characteristic of the viscous regime. (a) Initial acceleration phase with developing boundary layer. (b) Approach to terminal velocity exhibiting symmetric streamlines that, consistent with Stokes flow past a sphere. (c) Particle at  $0.5d$  from the domain bottom showing a fully developed symmetric flow field with smooth velocity decay to far-field values.

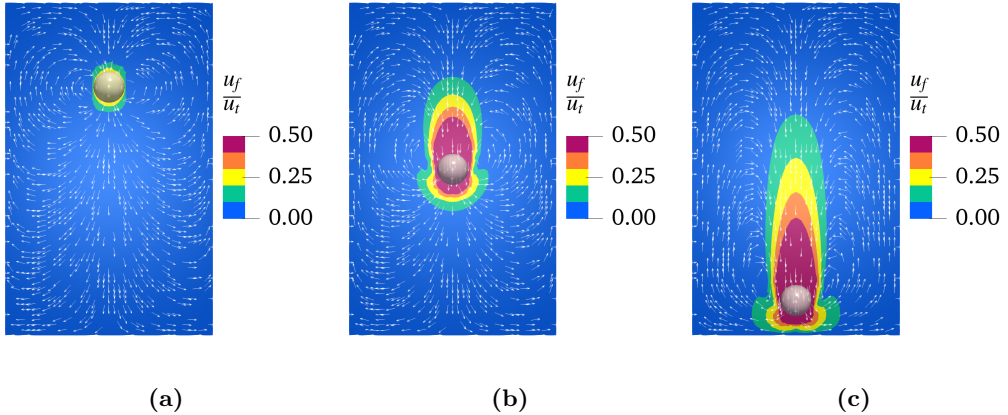


**Figure 4:** Velocity contours and streamlines for  $Re_p = 29.8$  (case 2) showing wake formation and flow separation characteristic of the inertial regime. (a) Initial acceleration phase. (b) Approach to terminal velocity with clear flow separation and wake region extending approximately  $1.0d$  downstream, indicating transition from viscous-dominated to inertia-dominated settling. (c) Particle at  $0.5d$  from the domain bottom, showing an established recirculating wake structure and an asymmetric pressure distribution that contributes to enhanced form drag.

### 3.2 Drafting, Kissing and Tumbling

The CFD-DEM capacity to resolve hydrodynamic interactions between multiple particles is verified through simulations of two settling spheres in quiescent fluid, following the benchmark configuration of [Glowinski et al. \[2001\]](#). The computational domain is a vertical rectangular box ( $10\text{ mm} \times 10\text{ mm} \times 40\text{ mm}$ ). Two identical spheres are released vertically, initially separated, and their settling velocities are tracked as they approach, collide, and tumble. [Figure 5](#) compares the settling velocity evolution of the two spherical particles with the direct numerical simulations (DNS) from [Sharma and Patankar \[2005\]](#), revealing three characteristic phases of particle-particle interactions:

- 1. Drafting—Independent settling regime ( $t < 0.14\text{ s}$ ):** The particles settle at identical velocities as the trailing particle remains beyond the wake of the leading particle. Each particle experiences drag from the undisturbed far-field flow, producing independent settling dynamics with a velocity difference of  $< 5\%$ .
- 2. Kissing—Wake entrainment regime ( $0.14\text{ s} < t < 0.35\text{ s}$ ):** The trailing particle enters the leading particle's wake, where streamwise fluid velocity is elevated relative to the far-field. The relative velocity between the fluid and the trailing particle reduces the drag force, leading to an apparent acceleration. The velocity difference causes rapid gap closure, bringing the particles to contact at  $0.35\text{ s}$ .
- 3. Tumbling—Collision and post-contact dynamics ( $t > 0.35\text{ s}$ ):** At  $t = 0.35\text{ s}$ , particles collide, the Hertz-Mindlin contact model calculates normal and tangential collision forces, resulting in particle tumbling and momentum exchange.

Quantitative comparison from the CFD-DEM shows good agreement with DNS benchmarks: maximum velocity deviation  $< 5\%$  throughout all phases, accurate prediction of collision time ( $0.35\text{ s}$ , within 5% of DNS), and correct post-collision behavior. The verification confirms that the IB method accurately resolves: (1) long-range wake-mediated

hydrodynamic interactions, (2) transition from independent to coupled settling, (3) contact collision dynamics, and (4) momentum transfer during tumbling. Flow field snapshots in [Figure 6](#) show particle positions and velocity contours at representative times of ( $t = 0.0\text{ s}$ ,  $0.14\text{ s}$ ,  $0.35\text{ s}$ ,  $0.7\text{ s}$ ), illustrating the progressive wake entrainment mechanism and collision-induced flow reorganization.

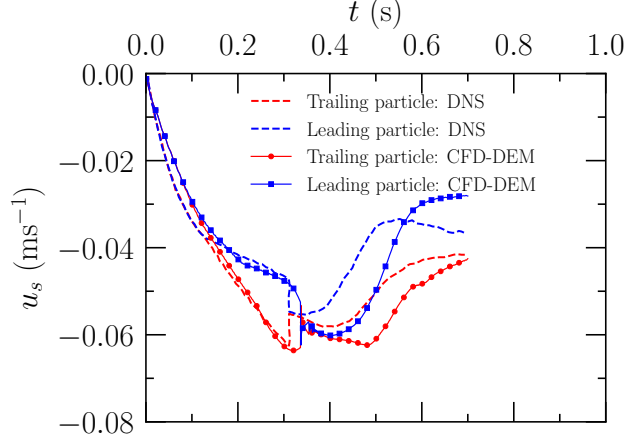


**Figure 5:** Comparison of settling velocity evolution for the two-particle drafting-kissing-tumbling benchmark. CFD-DEM predictions (solid lines) show good agreement with DNS results from [Sharma and Patankar \[2005\]](#) (dashed lines). The three characteristic phases are evident: drafting ( $t < 0.14\text{ s}$ ) with independent settling, kissing ( $0.14\text{ s} < t < 0.35\text{ s}$ ) with wake entrainment causing trailing particle acceleration and gap closure, and tumbling ( $t > 0.35\text{ s}$ ) following collision with momentum exchange. The maximum velocity deviation remains below 5% throughout the drafting and kissing phases, verifying the IB method for multi-particle hydrodynamic interactions.

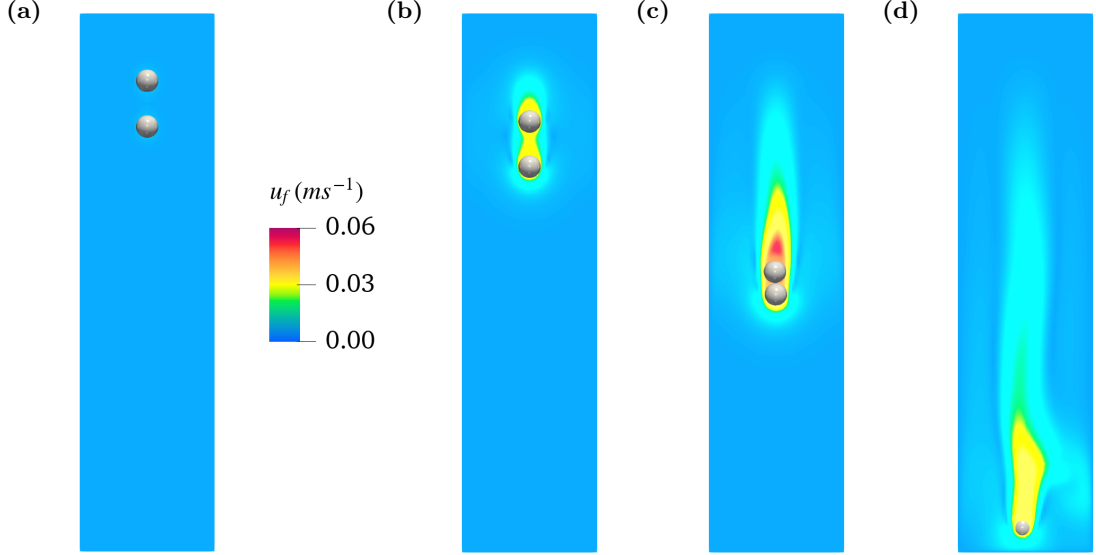


**Figure 6:** Particle positions and fluid velocity magnitude contours at representative times during particle sedimentation, illustrating the drafting-kissing-tumbling phenomenon. (a) 0 s: initial configuration with particles vertically aligned. (b) 0.14 s: onset of kissing phase as trailing particle enters leading particle's wake. (c) 0.35 s: particle collision with maximum velocity difference. (d) 0.7 s: post-collision tumbling with flow reorganization and momentum redistribution.

### 3.3 Non-spherical Particle Settling

The framework's suitability in handling complex particle morphologies is assessed through a sedimentation simulation of an idealized spherical particle, approximated using a multisphere approach. The test particle comprises 206 overlapping sub-spheres arranged to approximate a spherical geometry while maintaining identical density ( $\rho_s = 1120 \text{ kg m}^{-3}$ ) and volume, as the reference sphere from Case 2 ( $d = 15 \text{ mm}$ ). The configuration enables a direct comparison of the hydrodynamic behavior of a spherical particle with that of a non-spherical proxy under identical physical conditions. The computational setup maintains consistency with the verification case 2; fluid properties  $\rho_f = 960 \text{ kg m}^{-3}$  and  $\mu_f = 0.058 \text{ Pa} \cdot \text{s}$ , rectangular domain dimensions  $100 \times 100 \times 160 \text{ mm}^3$ , and particle is released from the same initial position. The mesh resolution is enhanced to  $d/\Delta x = 16$  (compared to 12 for the sphere) to ensure adequate representation of the irregular particle surface. Time step sizes remain unchanged at  $\Delta t_{\text{DEM}} = 1 \times 10^{-5} \text{ s}$  and  $\Delta t_{\text{CFD}} = 1 \times 10^{-4} \text{ s}$  to maintain temporal accuracy and numerical stability.

Figure 7 compares the settling velocity evolution for spherical and multisphere particles. The multisphere particle exhibits terminal velocity  $u_t = 0.12 \text{ m s}^{-1}$ , representing  $\leq 5\%$  decrease relative to the sphere ( $u_t = 0.128 \text{ m s}^{-1}$ ). Despite the irregular surface geometry, particles exhibit quantitatively similar acceleration dynamics, with a smooth, monotonic approach to terminal velocity over  $t \approx 0.8 \text{ s}$ . The subtle velocity decrease for the multisphere particle reflects enhanced drag due to its increased surface area, which is greater than that of the equivalent sphere. The flow field around the non-spherical particle exhibits wake structures similar to those in the spherical case, with symmetric streamlines characteristic of Stokes flow and no flow separation, see Figure 8. However, subtle asymmetries appear in the near-wall velocity contours, particularly downstream of surface protrusions where local velocity gradients intensify. These features reflect the particle's irregular geometry but do

not significantly alter the global force balance or settling dynamics at this low Reynolds number.

The close agreement between spherical and multisphere terminal velocities (within 5.0%) validates two critical aspects of the computational framework: (1) the multisphere approximation accurately represents the hydrodynamic resistance of irregular particles while maintaining computational efficiency, and (2) the IB method accurately resolves fluid-solid interactions around complex geometries with accuracy comparable to smooth surfaces. This verification provides confidence for subsequent investigations of PMN transport, where particle morphology significantly influences drag coefficients and suspension dynamics at higher Reynolds numbers ( $Re_p = 100\text{--}3000$ ).

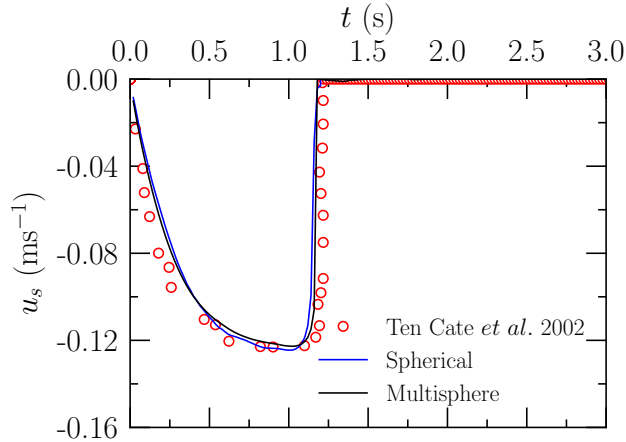


**Figure 7:** Settling velocity comparison between spherical and multisphere particles verifying the multisphere approximation. The test particle comprises 206 overlapping sub-spheres arranged to approximate the spherical geometry while maintaining identical density ( $\rho_s = 1120 \text{ kg m}^{-3}$ ), volume, and mass as the reference sphere from Case 2. The particles settle in silicon oil ( $\rho_f = 960 \text{ kg m}^{-3}$ ,  $\mu_f = 0.058 \text{ Pa} \cdot \text{s}$ ). Experimental data from [Ten Cate et al. \[2002\]](#) (red circles) provides the spherical particle baseline, while numerical predictions for the sphere (blue line) and multisphere assembly (black line) show close agreement with terminal velocity differences within 5%.

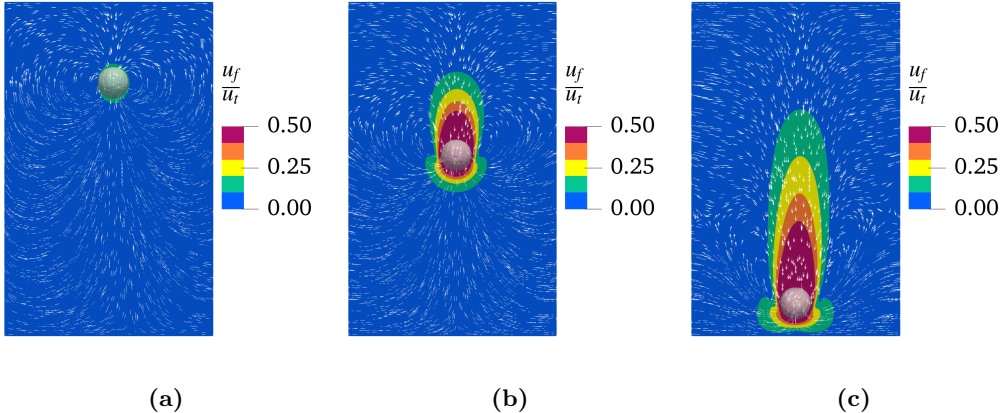


**Figure 8:** Flow field around multisphere particle during sedimentation, showing wake asymmetries due to irregular geometry. (a) initial phase. (b) Steady settling at terminal velocity exhibiting local velocity gradient intensifications near geometric irregularities while maintaining globally symmetric streamlines. (c) Near-wall interaction showing subtle flow perturbations induced by particle morphology.

#### 4 Results and Discussion

We systematically investigate the hydrodynamic behavior of PMNs in confined vertical flows, which is directly relevant to hydraulic lifting systems used in deep-sea mining risers. The analysis is structured in two parts. First, sedimentation in quiescent fluid is examined to quantify shape-induced drag enhancement and establish reference settling velocities for irregular PMNs relative to volume-equivalent spheres. These results provide calibration data for drag models commonly used in riser-scale simulations. Second, vertical hydraulic transport is analyzed using residence-time statistics and drag-force distributions to identify entrainment behavior and transport stability as flow velocity increases.

All transport simulations are performed with 40 particles to provide statistically meaningful ensemble measures while preserving fully resolved particle-fluid interactions. This particle number captures particle-to-particle variability without introducing collective effects such as sustained clustering or plug formation, which are beyond the scope of the present study. Continuous particle injection is not considered here; instead, the focus is on isolating the intrinsic hydrodynamic response of PMNs under controlled confinement. This approach enables clear physical interpretation and directly supports the reduced-order modeling strategies in the context of riser-scale transport.

##### 4.1 Settling Analysis

Figure 9 illustrates the complex and irregular morphology of PMNs represented using a multisphere approximation based on high-resolution CT scans. This approach employs 28 and 45 sub-spheres for PMNs with effective diameters of  $d_{\text{eff}} = 20 \text{ mm}$  and  $d_{\text{eff}} = 54 \text{ mm}$ , respectively, where  $d_{\text{eff}}$  represents the diameter of the minimum circumscribed sphere that fully encloses the PMNs. The volume-equivalent sphere diameter  $d_v = (6V_p/\pi)^{1/3}$ , where  $V_p$  is the actual particle volume, yields  $d_v = 16.4 \text{ mm}$  and  $d_v = 44 \text{ mm}$  for the small and large PMNs, respectively. The ratio  $(d_v/d_{\text{eff}})^3 \approx 0.55$  indicates that PMNs occupy only 55% of their circumscribed volume, reflecting their irregular, non-convex morphology with

surface protrusions and concavities characteristic of natural PMNs. The multisphere representations in [Figure 9b](#) and [d](#) show the PMN geometries superimposed with their volume-equivalent spheres, demonstrating that the irregular PMN surfaces extend significantly beyond the volume-equivalent sphere while remaining contained within the circumscribed sphere envelope. This geometric distinction is crucial for understanding hydrodynamic behavior, as the effective frontal area and surface morphology of PMNs differ substantially from volume-equivalent spheres.

[Figure 10](#) compares the temporal evolution of settling velocities for PMNs and their volume-equivalent spherical particles in fluid. The numerical simulations are performed within a cylindrical computational domain with diameter  $D = 200$  mm and length  $L = 1200$  mm. The mesh is constructed with resolution requirements based on the particle characteristic dimension: for PMNs, we use  $d_{\text{eff}}/\Delta x \geq 8$  to resolve surface irregularities and wake structures; for volume-equivalent spheres, we use  $d_v/\Delta x \geq 8$ . This ensures at least 8 grid cells across the particle dimension in all cases. Both PMNs and spherical particles have density  $\rho_p = 2000 \text{ kg m}^{-3}$  and identical volumes. They are released from rest at the domain centerline at height  $z = 1000$  mm in quiescent fluid with density  $\rho_f = 1000 \text{ kg m}^{-3}$  and dynamic viscosity  $\mu_f = 0.05 \text{ Pa} \cdot \text{s}$ . The terminal velocity  $u_t$  is determined from the steady-state settling velocity achieved after initial transients decay.

**Table 2:** Comparison of settling characteristics for PMNs and volume-equivalent spheres

Particle	$d_v$ (mm)	$d_{\text{eff}}$ (mm)	$u_t$ ( $\text{m s}^{-1}$ )	$Re_p$	$C_D$
Small sphere	16.4	16.4	0.45	148	1.01
Small PMN	16.4	20.0	0.30	98	2.28
Large sphere	44.0	44.0	1.05	924	0.44
Large PMN	44.0	54.0	0.75	660	0.86

Note:  $Re_p$  based on  $d_v$ ;  $C_D$  based on  $A_{\text{proj}} = \pi d_v^2/4$

[Figure 10](#) reveals that PMNs settle significantly slower than volume-equivalent spheres despite identical mass and buoyancy. The small PMN reaches terminal velocity  $u_t^{\text{PMN}} = 0.30 \text{ m s}^{-1}$  compared to  $u_t^{\text{sphere}} = 0.45 \text{ m s}^{-1}$  (33% reduction), while the large PMN achieves  $u_t^{\text{PMN}} = 0.75 \text{ m s}^{-1}$  versus  $u_t^{\text{sphere}} = 1.05 \text{ m s}^{-1}$  (29% reduction). These velocity differences are purely shape effects and correspond to  $Re_p$  of 98 and 148 (small PMN and sphere) and 660 and 924 (large PMN and sphere). The drag coefficient, defined from terminal force balance as  $C_D = 4(\rho_p - \rho_f)gd_v/(3\rho_f u_t^2)$  using the projected area  $A_{\text{proj}} = \pi d_v^2/4$ , yields  $C_D^{\text{PMN}} = 2.28$  and 0.86 compared to  $C_D^{\text{sphere}} = 1.01$  and 0.44 for small and large particles, respectively—representing 2.3 and 2.0 times enhancements [[Vergara et al., 2024](#)]. This drag increase primarily arises from the 50% larger surface area of PMNs relative to volume-equivalent spheres ( $(d_{\text{eff}}/d_v)^2 \approx 1.5$ ), supplemented by irregular particle morphology that creates asymmetric wake structures, see [Figure 11](#). Accounting for surface area differences through normalized drag coefficients  $C_D^{\text{norm}} = C_D^{\text{PMN}}(d_v/d_{\text{eff}})^2$  yields values still 20–30% above spherical equivalents, confirming shape-induced effects contribute greatly beyond confinement effects.

[Figure 12](#) shows the temporal evolution of vertical drag force during sedimentation, revealing distinct transient dynamics. The particle exhibits an increase during the initial acceleration phase due to added mass effects. The drag forces reach steady-state values of  $F_d = (\rho_p - \rho_f)V_p g \approx 0.0226 \text{ N}$  (small) and 0.44 N (large), confirming force balance to within 5%. Critically, both PMNs and spheres experience identical terminal drag forces since they have equal volumes and densities—the 29–33% lower settling velocities of PMNs arise

because their enhanced drag coefficients allow them to generate the required hydrodynamic resistance at reduced slip velocities. The sharp decrease in  $F_d$  after  $t \approx 2.8$  s for the small PMN indicates bottom contact, where wall reaction forces partially support the particle weight.

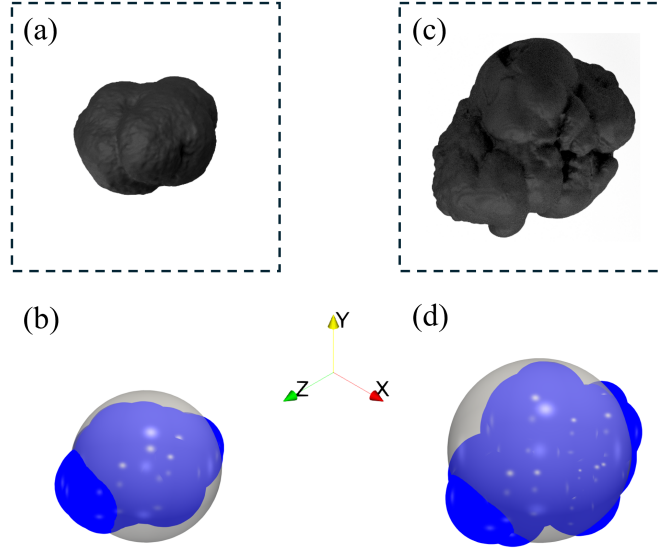


**Figure 9:** PMN morphology and multisphere approximations. (a) & (c) CT-reconstructed surfaces of PMNs showing irregular geometry characteristic of natural PMNs. (b) & (d) Multisphere representations (blue) comprising 28 and 45 sub-spheres for effective diameters  $d_{\text{eff}} = 20$  mm and 54 mm, respectively, superimposed on volume-equivalent spheres (grey,  $d_v = 16.4$  mm and 44 mm). The volume ratio  $(d_v/d_{\text{eff}})^3 \approx 0.55$  indicates that PMNs occupy only 55% of their circumscribed sphere volume due to non-convex morphology.

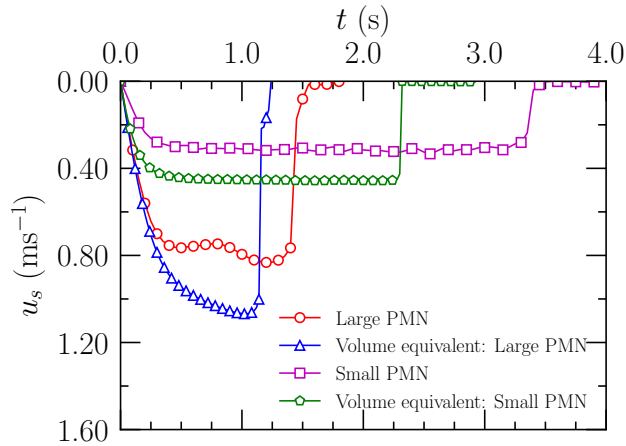


**Figure 10:** Temporal evolution of settling velocity for PMNs and volume-equivalent spherical particles. PMNs (squares and circles) reach terminal velocities 29–33% lower than volume-equivalent spheres (triangles and pentagons) despite identical mass and volume, reflecting enhanced drag coefficients due to increased surface area.

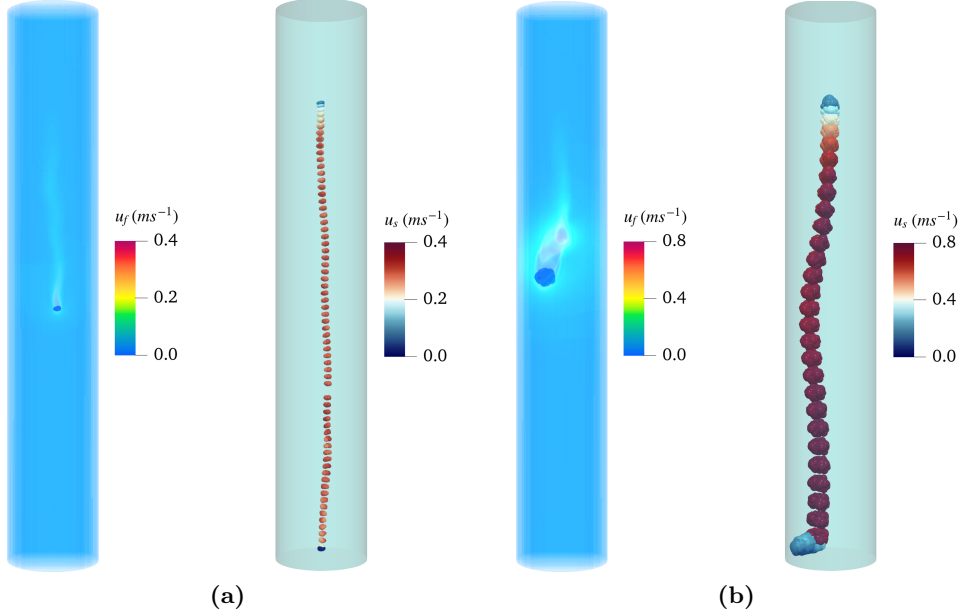


**Figure 11:** Instantaneous flow fields and particle trajectories during sedimentation of PMNs in quiescent fluid. (a) Small PMN at terminal velocity. (b) Large PMN. The fluid velocity magnitude contours show asymmetric wake structures resulting from irregular particle geometry (left). Three-dimensional particle trajectories colored by solid velocity magnitude, demonstrating vertical settling with coupled rotational motion (right).

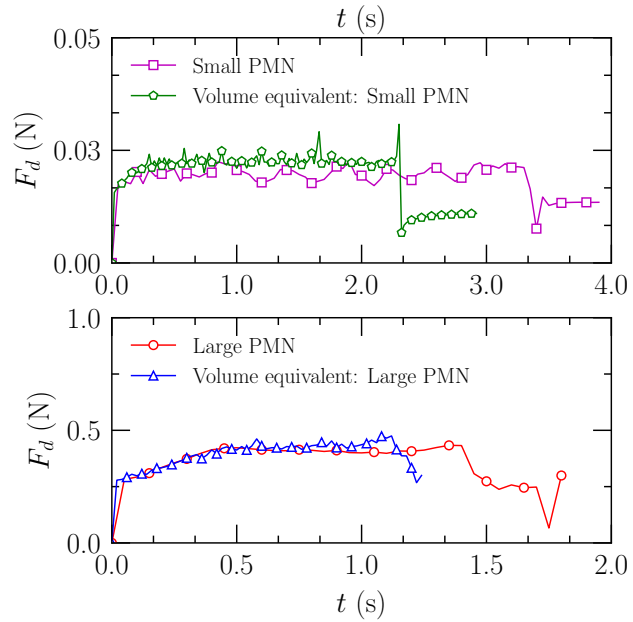


**Figure 12:** Temporal evolution of vertical drag force during sedimentation for PMNs and volume-equivalent spheres. Small particles reach steady-state drag force  $F_d \approx 0.023$  N (top). Large particles achieve  $F_d \approx 0.43$  N (bottom).

## 4.2 Vertical transport

To investigate PMN entrainment in vertical risers, we simulate the transport of mono-sized spherical particles ( $d_v = 16.4$  mm and 44 mm) through a vertical cylindrical pipe with diameter  $D = 200$  mm and length  $L = 1200$  mm at three fluid velocities:  $u_f = 1.0u_t$ ,  $2.0u_t$ , and  $3.0u_t$ , where  $u_t$  is the terminal settling velocity, [Table 3](#) lists the  $Re_p$  values. Particles are initially distributed randomly in the lower section of the pipe ( $0 < y < 200$  mm) and allowed to reach quasi-steady transport conditions. The flow Reynolds number ranges from  $Re_{\text{pipe}} = \rho_f u_f D / \mu_f \approx 1200\text{--}4000$ , placing the flow in the transitional to weakly turbulent regime. We analyze transport characteristics through residence time distributions  $P(t_r)$  and normalized drag force distributions  $P(\hat{f})$ , where  $t_r$  is the time required for a particle to traverse one meter vertically and  $\hat{f} = F_d / (\rho_p - \rho_f) V_{pg}$  is the ratio of instantaneous vertical drag to particle weight.

**Table 3:** Particles' Reynolds numbers ( $Re_p$ ) for spherical particles and PMNs during vertical transport at varying fluid velocities. Terminal velocities  $u_t$  from sedimentation analysis with  $\rho_f = 1000 \text{ kg m}^{-3}$  and  $\mu_f = 0.05 \text{ Pa} \cdot \text{s}$ .

Particle Type	$d_v$ (mm)	$u_t$ ( $\text{m s}^{-1}$ )	$Re_p = \rho_f u_f d_v / \mu_f$		
			$u_f = 1.0u_t$	$u_f = 2.0u_t$	$u_f = 3.0u_t$
Small sphere	16.4	0.42	138	276	414
Small PMN	16.4	0.30	98	196	294
Large sphere	44.0	1.1	968	1936	2904
Large PMN	44.0	0.80	704	1408	2112

Note:  $Re_p$  calculated using volume-equivalent diameter  $d_v$  and fluid velocity  $u_f$ .

### 4.2.1 Residence Time Analysis

[Figure 13](#) presents the probability distributions of residence time ( $t_r$ ) for spherical and non-spherical particles at varying flow velocities. The distributions characterize the transition from intermittent, settling-dominated transport at low velocities to steady, convection-dominated entrainment at high velocities. In [Figure 13a](#) and [c](#), the small spherical particles and PMNs, respectively, exhibit broad distributions with extended tails at  $u_f = 1.0u_t$  and  $u_f = 12.0u_t$ , indicating high variability in individual particle transport velocities. For spheres, the standard deviation decreases from  $\sigma_{tr} = 1.55 \text{ s}$  at  $1.0u_t$  to  $\sigma = 0.06 \text{ s}$  at  $3.0u_t$ . At  $1.0u_t$ , the small PMNs exhibit marginal suspension states—particles oscillate near the inlet without achieving consistent upward motion. This is illustrated in particle trajectory visualizations (see [Figure 14e](#) and [Figure 15e](#)), where small PMNs remain confined to the lower pipe section at low velocity, exhibiting continuous rotational motion without net vertical displacement. Large spherical particles, [Figure 13b](#), show systematic variance reduction from  $\sigma = 0.19 \text{ s}$  to  $\sigma = 0.02 \text{ s}$  as the fluid velocity increases. Large PMNs, [Figure 13d](#), exhibit broader distributions at all velocities compared to spherical particles, with more pronounced tails at  $2.0u_t$  and  $3.0u_t$ .

The mean residence times ( $\mu_{tr}$ ) for all particles follow the expected inverse relationship  $\mu_{tr} \propto 1/u_f$ , with measured values of  $\mu_{tr} = 6.87 \text{ s}$ ,  $1.85 \text{ s}$ , and  $1.04 \text{ s}$  for small spherical particles at  $1.0u_t$ ,  $2.0u_t$ , and  $3.0u_t$ , respectively. [Table 4](#) delineates the  $\mu_{tr}$  and  $\sigma_{tr}$  for various particle groups. Particle configuration snapshots in [Figure 14](#) reveal the spatial distributions underlying these statistical behaviors. At  $1.0u_t$ , small spherical particles, [Figure 14a](#) exhibit pronounced vertical dispersion with particles spanning the half pipe length, consistent with the broad residence time distribution and intermittent settling events. Small

PMNs (see [Figure 14e](#)) show extreme clustering near the inlet with minimal upward progression, confirming marginal suspension. Large particles, [Figure 14c](#) and [g](#), show less dispersion due to higher inertia, which reduces susceptibility to local flow fluctuations.

At  $3.0u_t$ , all particle types achieve spatially homogeneous distributions with minimal vertical dispersion, confirming efficient entrainment and stable transport (see [Figure 14b](#), [d](#), [f](#), and [h](#)). The absence of extended residence time tails at this velocity indicates that all particles maintain consistent upward motion without settling reversals. Flow field visualizations show that small PMNs develop subtle asymmetric wakes and helical trajectories with variable angular velocity even at high velocities, [Figure 14f](#), while large PMNs exhibit no complex wake structures with angular velocities reaching  $80 \text{ rad s}^{-1}$ , [Figure 14h](#). Individual particle trajectories in [Figure 15](#) provide a direct visualization of these transport regimes. Small spherical particles ([Figure 15a](#) and [b](#)) transition from oscillatory motion with lateral wandering at  $1.0u_t$  to nearly rectilinear trajectories at  $3.0u_t$ . However, the Small PMNs ([Figure 15e](#)) remain in marginal suspension at low velocity. Large PMNs, [Figure 15g](#) and [h](#), exhibit enhanced rotational motion, with PMNs achieving significantly higher angular velocities, reflecting shape-induced torques and coupled translational-rotational dynamics.

**Table 4:** Mean residence time ( $\mu_{tr}$ ) and standard deviation ( $\sigma_{tr}$ ) for spherical particles and PMNs during vertical transport at varying fluid velocities.

Particle	$\mu_{tr}$ (s)			$\sigma_{tr}$ (s)		
	$1.0u_t$	$2.0u_t$	$3.0u_t$	$1.0u_t$	$2.0u_t$	$3.0u_t$
Small sphere	6.87	1.85	1.04	1.55	0.18	0.06
Small PMN	—	3.51	1.62	—	0.75	0.11
Large sphere	1.48	0.52	0.33	0.19	0.04	0.02
Large PMN	2.11	0.89	0.51	0.39	0.10	0.06

Note: Small PMNs remain in a suspended state at  $1.0u_t$

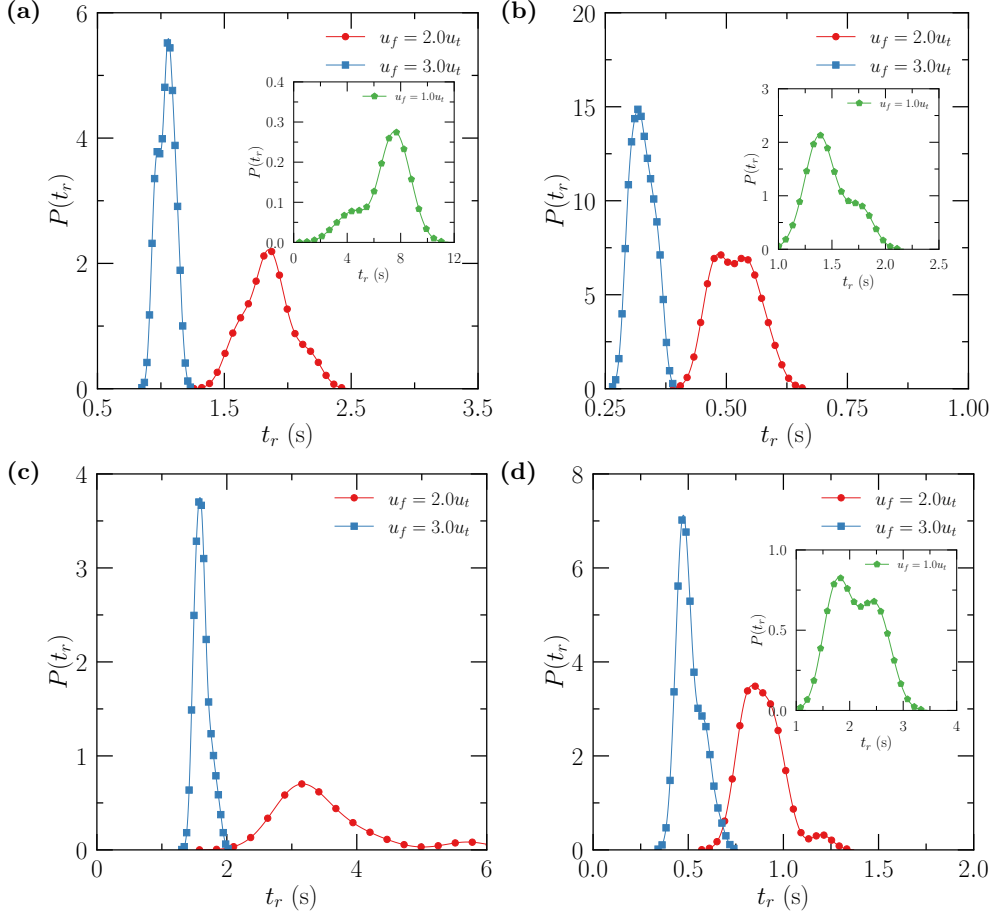


**Figure 13:** Probability distributions of residence time  $t_r$  at fluid velocities  $u_f = 1.0u_t$ ,  $2.0u_t$ , and  $3.0u_t$ . (a) Small spheres. (b) Large spheres. (c) Small PMNs. (d) Large PMNs. The distributions narrow systematically with increasing velocity, transitioning from broad, variance-dominated profiles at low flow rates (insets) to sharp, convection-dominated distributions at high rates. Note: Small PMNs remain suspended at  $u_f = 1.0u_t$  without net upward transport.

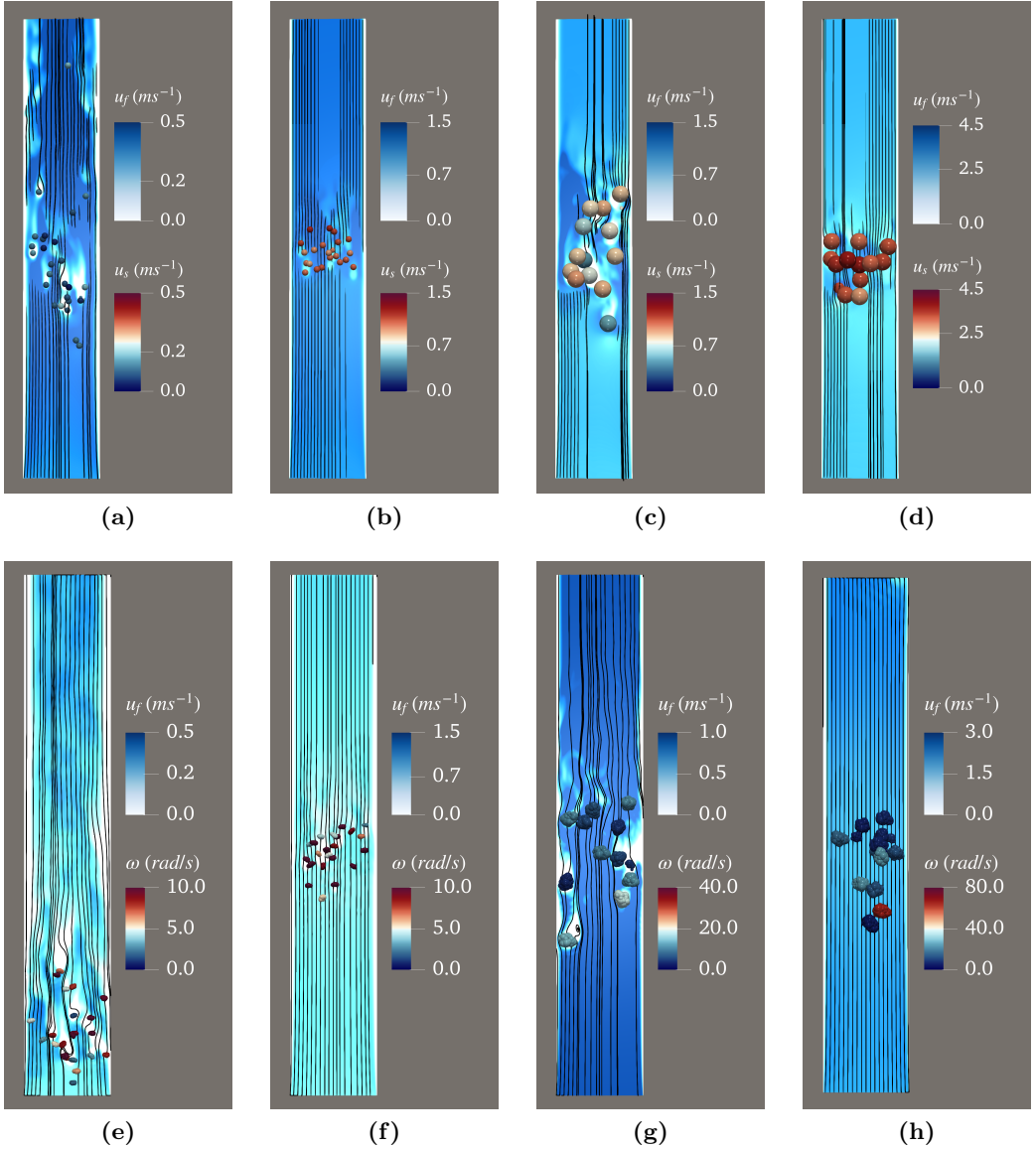


**Figure 14:** Particle configurations and flow fields during vertical transport. Small spheres ( $d_v = 16.4 \text{ mm}$ ): (a)  $u_f = 1.0u_t$  shows vertical dispersion and lateral spread; (b)  $u_f = 3.0u_t$  shows homogeneous distribution with rectilinear motion. Large spheres ( $d_v = 44 \text{ mm}$ ): (c)  $u_f = 1.0u_t$  shows moderate dispersion; (d)  $u_f = 3.0u_t$  shows homogeneous distribution. Small PMNs: (e)  $u_f = 1.0u_t$  shows asymmetric wakes and helical trajectories; (f)  $u_f = 3.0u_t$  shows reduced dispersion with continued rotational motion. Large PMNs: (g)  $u_f = 1.0u_t$  shows complex wake structures; (h)  $u_f = 3.0u_t$  shows linear trajectories with angular velocity up to  $80 \text{ rad s}^{-1}$  and intermittent wall-proximity events. Fluid velocity is colored by magnitude, and streamlines are shown as tube elements (left). Particle trajectories colored by velocity (top right rows) or angular velocity (bottom right rows).

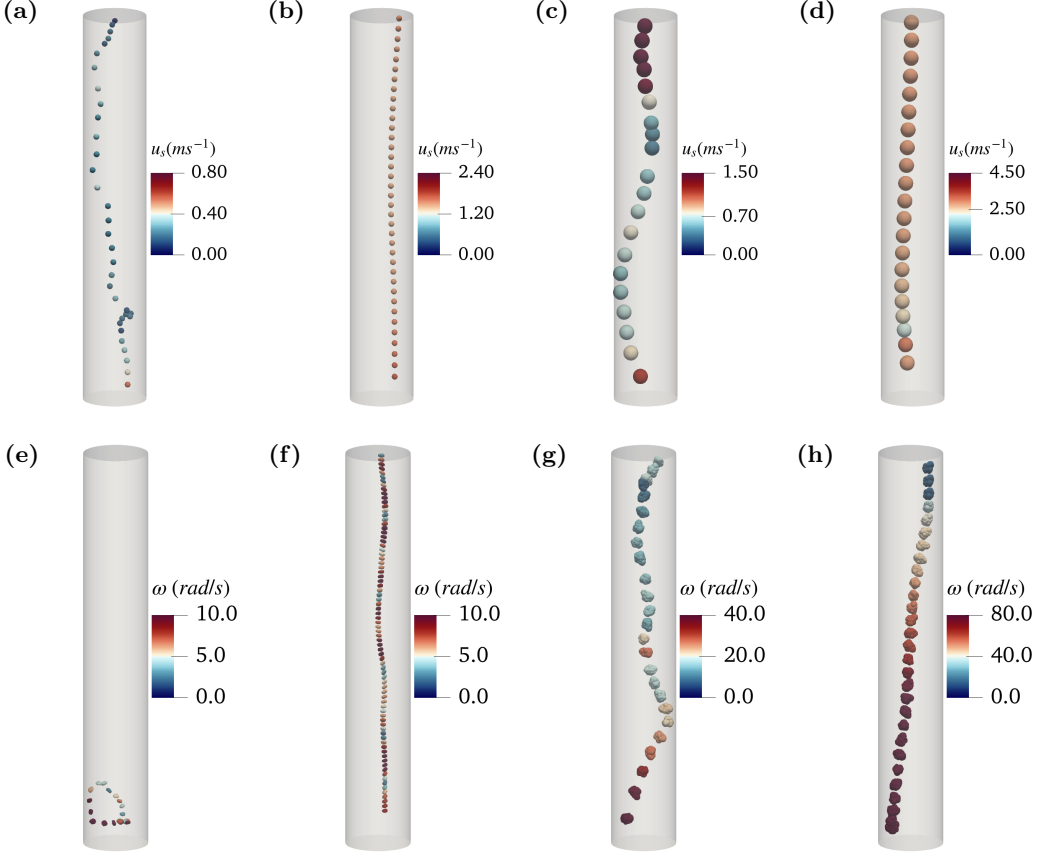


**Figure 15:** Particle trajectory for a random particle during vertical hydraulic transport, colored by instantaneous translational ( $u_s$ ) or angular velocity ( $\omega$ ). Small particles with (a) & (b) as spheres and (e) & (f) as PMNs at  $u_f = 1.0u_t$  and  $3.0u_t$ , respectively, colored by translational ( $u_s$ ) or angular ( $\omega$ ) velocity. The small PMNs remain in a state of marginal suspension near the pipe inlet, exhibiting oscillatory motion without net upward transport—the fluid velocity is insufficient to overcome gravitational settling, resulting in a dynamic equilibrium in which the particles hover with continuous rotational adjustments. Large particles with (c) & (d) as spheres and (g) & (h) as PMNs at  $u_f = 1.0u_t$  and  $3.0u_t$ , respectively. At low flow velocity ( $u_f = 1.0u_t$ ), trajectories exhibit significant lateral dispersion and velocity fluctuations reflecting intermittent transport. At high flow velocity ( $u_f = 3.0u_t$ ), trajectories become more vertically aligned with reduced dispersion, indicating stable convection-dominated transport. The PMNs exhibit enhanced rotational motion due to shape-induced torque than volume-equivalent spheres.

#### 4.2.2 Drag Force Analysis

Figure 16a and b illustrate the probability distributions of the normalized axial drag force,  $\hat{f} = F_d/(\rho_p - \rho_f)V_p g$ , providing insight into the force balance mechanisms governing particle suspension. Across all fluid velocities examined, the mean normalized drag force remains approximately near one (i.e.,  $\langle \hat{f} \rangle \approx 1$ ), confirming that drag effectively balances particle weight under steady-state conditions. Particles continuously adjust their slip velocity to maintain this equilibrium, regardless of the imposed fluid velocity. This behavior aligns with classical multiphase flow theory, where terminal velocity defines the threshold for suspension, and higher entrainment velocities enhance stability without significantly altering the mean force balance. While gravitational and hydrodynamic forces remain dynamically balanced on average, the distinction between different operating conditions arises from the

shape of the distributions, which encapsulate the fluctuating components of the drag force and their dependence on turbulence, inertia, and confinement.

The evolution of drag-force statistics can be directly interpreted in light of the resolved flow fields shown in [Figure 14](#). For the smaller spherical particles, at  $u_f = u_t$ , the flow exhibits clear local velocity deficits and moderate streamline curvature around individual particles, indicating the presence of short, attached wakes, see [Figure 14a](#). In this regime, the particle inertia is low ( $St \approx 30.6$ ), such that particle motion remains strongly coupled to the carrier flow and rapidly adapts to local velocity fluctuations [[Balachandar and Eaton, 2010](#)]. The Stokes number  $St$  is defined as

$$St = \frac{\rho_p d_v u_t}{9\mu_f}. \quad (7)$$

As a result, drag fluctuations remain weak, and the corresponding force distribution is narrow, [Figure 16a](#). As the flow velocity increases to  $u_f = 3u_t$ , the streamline patterns appear straighter and individual wake structures become less visually distinct, [Figure 14b](#). This does not imply the absence of wake dynamics. Instead, the increase in  $Re_p$  leads to wake structures that are rapidly convected downstream, while axial shear and inter-particle interactions inhibit the formation of spatially coherent recirculation zones [[Crowe et al., 2011](#)]. In this regime, wake-induced disturbances persist but are temporally short-lived and not spatially localized, resulting in a modest broadening of the drag-force distribution without significant intermittency.

A qualitatively different behavior is observed for the larger spherical particles ( $d_v = 44\text{ mm}$ ). At  $u_f = u_t$ , the flow field reveals strong streamline distortion and a pronounced velocity deficit downstream of the particle cluster. The wake remains coherent and visibly asymmetric due to lateral confinement by the pipe wall ( $d_v/D = 0.220$ ), but adjusts quasi-steadily to particle motion. Such confinement-induced wake asymmetry and deflection are well documented for bluff bodies in pipes and channels [[Zdravkovich, 1997](#), [Sahin and Owens, 2004](#)]. Despite the higher particle inertia ( $St \approx 215$ ), the quasi-steady wake adjustment yields relatively narrow distributions of drag force, see [Figure 16b](#). At  $u_f = 3u_t$ , the instantaneous flow visualizations show predominantly axial streamlines with no clearly identifiable recirculation [Figure 14d](#). This apparent suppression of wake structures does not indicate steady drag conditions. At high inertia ( $St \approx 645$ ) and elevated  $Re_p$ , wake dynamics transition to a regime dominated by rapid downstream convection, confinement-induced suppression of lateral wake expansion, and strong interactions with neighboring particles and the confining wall [[Zdravkovich, 1997](#)]. Under these conditions, the particle response time becomes comparable to the characteristic time scales of wake evolution, resulting in history-dependent drag forces that are not uniquely determined by the instantaneous slip velocity [[Balachandar and Eaton, 2010](#), [Leskovec et al., 2024](#)]. Consequently, drag fluctuations become intermittent and heavy-tailed, even though wake structures are not readily apparent in instantaneous streamline plots.

The drag force distribution for small PMNs in [Figure 16c](#) exhibits behavior quantitatively similar to that of spherical particles, with sharp peaks centered around  $\hat{f} \approx 1.1 - 1.3$  across all flow velocities. This indicates that, for small particles, geometric irregularity plays a secondary role relative to inertia and confinement. Owing to their low effective inertia and rapid rotational dynamics, small PMNs remain strongly coupled to the carrier flow, such that orientation-dependent variations in projected area are rapidly averaged out and drag fluctuations are primarily governed by local flow variability. In contrast, the drag-force distributions for large PMNs, [Figure 16d](#), exhibit distinct features associated with orientation-dependent forcing. At  $1.0u_t$ , the distribution is relatively narrow but shifted

toward higher values, with a peak at  $\hat{f} \approx 1.5$  and a tail extending to  $\hat{f} \approx 2.0$ , reflecting enhanced form drag associated with non-spherical geometry. As the flow velocity increases to  $2.0u_t$  and  $3.0u_t$ , the distributions broaden and shift toward  $\hat{f} \approx 1.7$ , accompanied by extended high-drag tails. At  $3.0u_t$ , the distribution becomes more sharply peaked than at intermediate velocities, yet remains substantially broader than that of spherical particles and retains a long tail extending to  $\hat{f} \approx 4.0$ .

Across all velocities, both small spheres and small PMNs maintain narrow, peaked distributions, whereas pronounced differences between spherical and non-spherical particles emerge for the larger size class. Large spherical particles exhibit a monotonic broadening of the drag distribution with increasing velocity, consistent with wake unsteadiness modified by confinement. For large PMNs, drag variability is further amplified by orientation-dependent forcing, which introduces an additional source of intermittency beyond wake dynamics alone. At  $1.0u_t$ , large PMNs experience irregular translational and rotational motion, including intermittent settling, wall-proximity events, and re-entrainment, leading to strong drag fluctuations. Flow-field visualizations in [Figure 14g](#) reveal complex three-dimensional wake structures with multiple separation points arising from the non-convex particle morphology. Particle trajectory snapshots (see [Figure 15](#)) confirm irregular lateral motion and variable angular velocity with intermittent wall-proximity events at low velocities. At higher velocities, increased angular velocity promotes more rapid reorientation and sustained transport upward through a more uniform mean flow. Although wake structures become less visually distinct due to rapid convection and confinement, orientation-induced variations in projected area persist, giving rise to intermittent high-drag events and the extended tails observed in [Figure 16d](#).

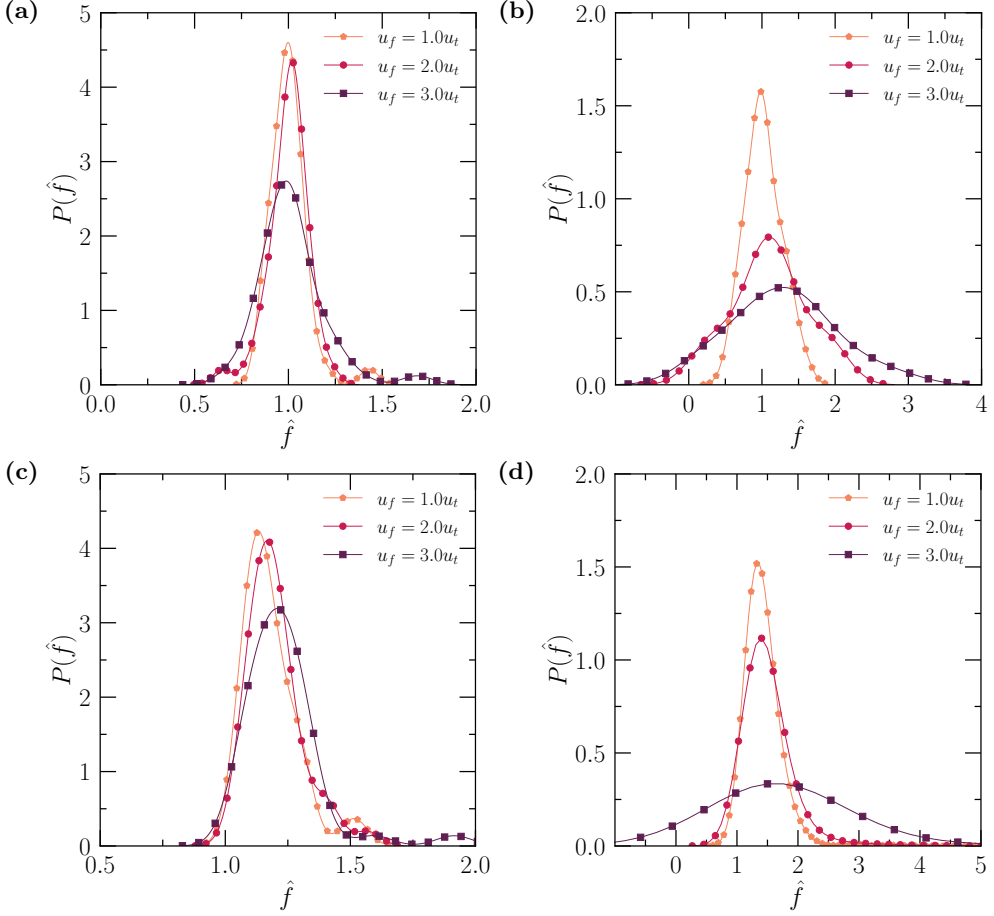


**Figure 16:** Probability distributions of normalized drag force,  $\hat{f} = F_d/m_p g$ , for spherical and non-spherical particles. (a) Small spherical particles. (b) Large spherical particles. (c) Small non-spherical PMNs (d) Large non-spherical PMNs.

## 5 Summary and Conclusions

This study employed a fully resolved CFD-DEM approach to investigate the hydrodynamic behavior of irregular polymetallic nodules (PMNs) during sedimentation and vertical hydraulic transport in confined risers, which are relevant to deep-sea mining operations. By explicitly resolving particle-fluid interactions without empirical drag closures. The simulations provide mechanistic insight into how particle shape, confinement, and flow velocity collectively govern settling dynamics, residence time statistics, and fluctuations in drag force across low to moderate  $Re_p$ . The key findings are outlined below.

1. Shape-induced drag enhancement governs PMN sedimentation, leading to reduced terminal velocities without altering the terminal force balance. Sedimentation simulations demonstrate that PMNs settle 29-33% slower than volume-equivalent spheres, irrespective of having the same mass and buoyancy. This reduction arises from an increase in the drag coefficient and morphology-induced wake asymmetry. Remarkably, the PMNs and spheres experience identical terminal drag forces equal to their submerged weight. The reduced settling velocity of PMNs reflects that the irregular particles generate the required hydrodynamic resistance at lower slip velocities, rather than an alteration in the equilibrium force balance.

2. The residence time distributions ( $t_r$ ) highlight a velocity-driven transition from intermittent to convection-dominated transport, particularly showing that non-spherical particles experience delayed entrainment. At low flow velocities, the spherical particles and PMNs display broad  $t_r$  indicative of intermittent motion and partial settling, with small PMNs remaining marginally suspended and exhibiting oscillatory trajectories. As flow velocity increases, these distributions narrow and peak, signifying a shift to stable convection-dominated transport. The PMNs demonstrate larger mean residence times and variances compared to spherical particles under similar flow conditions, which is attributable to the greater drag ( $\hat{f} > 1$ ) and rotational-translational coupling that contribute to the delayed entrainment.
3. Drag force statistics are significantly influenced by particle morphology and confinement, with non-spherical particles amplifying unsteady force fluctuations. The mean normalized drag force fluctuates around  $\hat{f} = 1 - 1.5$  across configurations, indicating a steady transport equilibrium between hydrodynamic drag and submerged weight. Distinct transport regimes are characterized by variations in drag fluctuations. Small particles exhibit narrow distributions in drag fluctuations, which aligns with their rapid response to flow changes and low Stokes number dynamics. In contrast, large particles at high confinement ratios exhibit non-monotonic drag statistics, characterized by increased force fluctuations at higher velocities. For PMNs, the interplay of orientation-dependent drag and shape-induced rotation further expands drag distributions.

While PMNs exhibit 40-90% longer residence times and 2 times higher drag coefficients compared to volume-equivalent spheres, the underlying transport physics remains qualitatively similar. Both particle types undergo the same progression from a settling transitional convection-dominated regime as flow velocity increases. This suggests that first-order transport behavior can be captured using volume-equivalent spherical particles with appropriately calibrated drag laws, though quantitative predictions require shape-specific corrections. Future work will extend this framework to polydisperse systems with continuous particle injection and quantify pressure drop and transport efficiency under realistic operating conditions.

### Acknowledgements

RKA acknowledges the financial support from National Institute of Ocean Technology, Ministry of Earth Sciences, Government of India.

### Conflict of Interest

The authors declare that they have no conflict of interest.

### References

- J. R. Hein, A. Koschinsky, T. Kuhn, Deep-ocean polymetallic nodules as a resource for critical materials, *Nature Reviews Earth & Environment* 1 (2020) 158–169.
- D. Leng, S. Shao, Y. Xie, H. Wang, G. Liu, A brief review of recent progress on deep sea mining vehicle, *Ocean Engineering* 228 (2021) 108565.
- J. Van Wijk, A. Talmor, C. van Rhee, Stability of vertical hydraulic transport processes for deep ocean mining: An experimental study, *Ocean Engineering* 125 (2016) 203–213.
- Y. Dai, Y. Zhang, Y. Cheng, J. Chen, X. Zhu, Cfd-dem simulation and experimental investigations on continuous hydraulic sampling of deep-sea polymetallic nodules, *Ocean Engineering* 313 (2024) 119509.

X. Su, B. Chen, H. Yang, Y. Ren, H. Wang, R. Lin, Effects of nozzle angles of a double-row jet collector on harvesting performance, *Ocean Engineering* 301 (2024) 117573.

W. Chen, H.-L. Xu, N. Peng, D. Hu, Q. Hao, Y. Xiao, Deep-sea mining ore collection model and pipeline system dynamic analysis, *Ocean Engineering* 342 (2025) 122892.

C. Yang, H. Qiu, R. Jin, H. Chen, G. Ma, Y. Hu, S. Sun, Numerical simulation of hydraulic lifting of multi-sized coarse particles in laterally vibrated pipe for deep-sea mining, *Physics of Fluids* 37 (2025).

Z. Shen, G. Wang, D. Huang, F. Jin, A resolved cfd-dem coupling model for modeling two-phase fluids interaction with irregularly shaped particles, *Journal of Computational Physics* 448 (2022) 110695.

E. A. Schnorr Filho, N. C. Lima, E. M. Franklin, Resolved cfd-dem simulations of the hydraulic conveying of coarse grains through a very-narrow elbow, *Powder Technology* 395 (2022) 811–821.

R. Zhao, Y. Zhou, D. Zhang, X. Gao, Numerical investigation of the hydraulic transport of coarse particles in a vertical pipe based on a fully-coupled numerical model, *International Journal of Multiphase Flow* 155 (2022) 104094.

X. Sun, L. Li, Z. Zhu, Z. Lin, Transition mechanisms of multi-scale particle flow regimes in hydraulic lifting pipes influenced by fluid velocity and particle concentration, *Powder Technology* (2025) 121820.

L. Yang, X. Chen, L. Luo, X. Wu, F. Jing, Effect of particle parameters on the hydraulic transport characteristics in a vertical pipeline for deep-sea mining, *Ocean Engineering* 321 (2025) 120408.

Z. Liu, K. Liu, X. Chen, Z. Ma, R. Lv, C. Wei, K. Ma, Deep-sea rock mechanics and mining technology: State of the art and perspectives, *International Journal of Mining Science and Technology* 33 (2023) 1083–1115.

Z. Li, H. Chen, Y. Wu, Z. Xu, H. Shi, P. Zhang, Cfd-dem analysis of hydraulic conveying of non-spherical particles through a vertical-bend-horizontal pipeline, *Powder Technology* 434 (2024) 119361.

R. Zhang, Y. Wang, L. Liu, X. Guo, Y. Liu, H. Liu, One-dimensional model for vertical hydraulic transport of high-concentration mineral particles, *Physics of Fluids* 36 (2024).

Z. Zhou, S. Kuang, K. Chu, A. Yu, Discrete particle simulation of particle–fluid flow: model formulations and their applicability, *Journal of Fluid Mechanics* 661 (2010) 482–510.

Z. Zhou, D. Pinson, R. Zou, A. Yu, Discrete particle simulation of gas fluidization of ellipsoidal particles, *Chemical Engineering Science* 66 (2011) 6128–6145.

F. Elskamp, H. Kruggel-Emden, M. Hennig, U. Teipel, A strategy to determine dem parameters for spherical and non-spherical particles, *Granular Matter* 19 (2017) 46.

D. Fan, H. Hou, J. Zeng, B. Yuan, Z. Lv, Y. Chen, Y. Li, S. Huang, A. Striolo, D. Zhang, Lattice boltzmann method/computational fluid dynamics-discrete element method applications for transport and packing of non-spherical particles during geo-energy explorations: A review, *Physics of Fluids* 36 (2024).

B. Chen, Y. Ren, X. Su, H. Wang, H. Chen, Particle dynamics analysis of hydraulic collecting for deep-sea mining based on overlapping mesh method, *Physics of Fluids* 37 (2025) 063354.

Y.-M. Huang, Y.-H. Sun, Z. Chen, The hydraulic conveying of coarse particles in pipelines: Flow characteristics and the critical non-deposition velocity, *Physics of Fluids* 37 (2025).

A. Haider, O. Levenspiel, Drag coefficient and terminal velocity of spherical and nonspherical particles, *Powder Technology* 58 (1989) 63–70.

G. H. Ganser, A rational approach to drag prediction of spherical and nonspherical particles, *Powder Technology* 77 (1993) 143–152.

A. Hölzer, M. Sommerfeld, New simple correlation formula for the drag coefficient of non-spherical particles, *Powder Technology* 184 (2008) 361–365.

Q. Chen, T. Xiong, X. Zhang, P. Jiang, Study of the hydraulic transport of non-spherical particles in a pipeline based on the cfd-dem, *Engineering Applications of Computational Fluid Mechanics* 14 (2020) 53–69.

H. Diamant, Hydrodynamic interaction in confined geometries, *Journal of the Physical Society of Japan* 78 (2009) 041002–041002.

K. Suresh, A. Kannan, Effects of particle diameter and position on hydrodynamics around a confined sphere, *Industrial & Engineering Chemistry Research* 50 (2011) 13137–13160.

G. Bagheri, C. Bonadonna, On the drag of freely falling non-spherical particles, *Powder Technology* 301 (2016) 526–544.

X. Cheng, Z. Cao, J. Li, A. Borthwick, A numerical study of the settling of non-spherical particles in quiescent water, *Physics of Fluids* 35 (2023).

R. Di Felice, The voidage function for fluid-particle interaction systems, *International Journal of Multiphase Flow* 20 (1994) 153–159.

J. Zhao, T. Shan, Coupled cfd-dem simulation of fluid–particle interaction in geomechanics, *Powder Technology* 239 (2013) 248–258.

K. Malone, B. Xu, Particle-scale simulation of heat transfer in liquid-fluidised beds, *Powder Technology* 184 (2008) 189–204.

X. Nan, J. Hou, Z. Shen, Y. Tong, G. Li, X. Wang, Y. Kang, Cfd-dem coupling with multi-sphere particles and application in predicting dynamic behaviors of drifting boats, *Ocean Engineering* 247 (2022) 110368.

M. Sommerfeld, Modelling of particle-wall collisions in confined gas-particle flows, *International Journal of Multiphase Flow* 18 (1992) 905–926.

C. Aponte-Rivera, R. N. Zia, Simulation of hydrodynamically interacting particles confined by a spherical cavity, *Physical Review Fluids* 1 (2016) 023301.

J. Chen, J. Li, Prediction of drag coefficient and ultimate settling velocity for high-density spherical particles in a cylindrical pipe, *Physics of Fluids* 32 (2020) 053303.

K. Luo, Z. Wang, J. Fan, A modified immersed boundary method for simulations of fluid-particle interactions, *Computer Methods in Applied Mechanics and Engineering* 197 (2007) 36–46.

J. Lu, M. D. Tan, E. A. Peters, J. A. Kuipers, Direct numerical simulation of reactive fluid-particle systems using an immersed boundary method, *Industrial & Engineering Chemistry Research* 57 (2018) 15565–15578.

H. Yan, D. Wang, G. Zhang, D. Wei, F. Liu, Complex fluid interface dynamics in water exit by improved diffuse interface-immersed boundary method, *Physics of Fluids* 37 (2025).

F. D. Cúñez, E. Franklin, Plug regime in water fluidized beds in very narrow tubes, *Powder Technology* 345 (2019) 234–246.

F. D. Cúñez, E. M. Franklin, Crystallization and jamming in narrow fluidized beds, *Physics of Fluids* 32 (2020).

Z. Lai, J. Zhao, S. Zhao, L. Huang, Signed distance field enhanced fully resolved cfd-dem for simulation of granular flows involving multiphase fluids and irregularly shaped particles, *Computer Methods in Applied Mechanics and Engineering* 414 (2023) 116195.

X. Nan, Z. Shen, J. Hou, G. Li, High-resolution model of complexly shaped bodies motion using an ibm-vof-dem coupling method, *Powder Technology* 413 (2023) 118005.

G. Hu, B. Zhou, Z. Shen, H. Wang, W. Zheng, A resolved cfd-dem investigation on granular sand sedimentation considering realistic particle shapes, *Géotechnique* (2024) 1–13.

K. Chen, P. Bachmann, A. Bück, M. Jacob, E. Tsotsas, Cfd simulation of particle residence time distribution in industrial scale horizontal fluidized bed, *Powder technology* 345 (2019) 129–139.

B. Lan, J. Xu, P. Zhao, Z. Zou, Q. Zhu, J. Wang, Long-time coarse-grained cfd-dem simulation of residence time distribution of polydisperse particles in a continuously operated multiple-chamber fluidized bed, *Chemical Engineering Science* 219 (2020) 115599.

C. Kloss, C. L. Goniva, A new open source discrete element simulation software, in: Proceedings of 5<sup>th</sup> international conference on discrete element methods, 2010, pp. 25–26.

R. D. Mindlin, H. Deresiewicz, Elastic spheres in contact under varying oblique forces, *Journal of Applied Mechanics* (1953).

A. Hager, C. Kloss, S. Pirker, C. Goniva, Parallel open source cfd-dem for resolved particle-fluid interaction, in: Proceedings of 9th International Conference on Computational Fluid Dynamics in Minerals and Process Industries, CSIRO Melbourne, Australia, 2012, pp. 1–6.

A. Ten Cate, C. Nieuwstad, J. J. Derkx, H. Van den Akker, Particle imaging velocimetry experiments and lattice-boltzmann simulations on a single sphere settling under gravity, *Physics of Fluids* 14 (2002) 4012–4025.

R. Glowinski, T.-W. Pan, T. I. Hesla, D. D. Joseph, J. Periaux, A fictitious domain approach to the direct numerical simulation of incompressible viscous flow past moving rigid bodies: application to particulate flow, *Journal of Computational Physics* 169 (2001) 363–426.

N. Sharma, N. A. Patankar, A fast computation technique for the direct numerical simulation of rigid particulate flows, *Journal of Computational Physics* 205 (2005) 439–457.

Á. Vergara, D. Wei, R. Fuentes, Drag coefficient for irregularly shaped grains: rotational dependence at various reynolds numbers, *Journal of Fluid Mechanics* 994 (2024) A1.

S. Balachandar, J. K. Eaton, Turbulent dispersed multiphase flow, *Annual review of fluid mechanics* 42 (2010) 111–133.

C. T. Crowe, J. D. Schwarzkopf, M. Sommerfeld, Y. Tsuji, *Multiphase Flows with Droplets and Particles*, volume 2nd Edition, CRC Press, 2011.

M. M. Zdravkovich, *Flow around circular cylinders: Volume 2: Applications*, volume 2, Oxford University Press, 1997.

M. Sahin, R. G. Owens, A numerical investigation of wall effects up to high blockage ratios on two-dimensional flow past a confined circular cylinder, *Physics of fluids* 16 (2004) 1305–1320.

M. Leskovec, S. Zade, M. Niazi, P. Costa, F. Lundell, L. Brandt, Turbulent pipe flow with spherical particles: Drag as a function of particle size and volume fraction, *International Journal of Multiphase Flow* 179 (2024) 104931.